

Enhancement of Electric Drive in Silicon Quantum Dots with Electric Quadrupole Spin Resonance

Philip Y. Mai,^{1,2,*} Pedro H. Pereira,^{3,*} Lucas Andrade Alonso,^{3,*} Ross C. C. Leon,^{1,†} Chih Hwan Yang,^{1,2} Jason C. C. Hwang,¹ Daniel Dunmore,¹ Julien Camirand Lemyre,⁴ Tuomo Tantt, ^{1,2} Wister Huang,^{1,‡} Kok Wai Chan,^{1,2} Kuan Yen Tan,^{1,§} Jesús D. Cifuentes,^{1,2} Fay E. Hudson,^{1,2} Kohei M. Itoh,⁵ Arne Laucht,^{1,2} Michel Pioro-Ladrière,^{4,6} Christopher C. Escott,^{1,2} MengKe Feng,^{1,2,¶} Reinaldo de Melo e Souza,³ Andrew Dzurak,^{1,2} and Andre Saraiva^{1,2,**}

¹*School of Electrical Engineering and Telecommunications,
The University of New South Wales, Sydney, NSW 2052, Australia*

²*Diraq, Sydney, NSW 2052, Australia*

³*Instituto de Física, Universidade Federal Fluminense, 24210-346, RJ, Brazil*

⁴*Institut Quantique et Département de Physique,
Université de Sherbrooke, Sherbrooke, Québec, J1K 2R1, Canada*

⁵*School of Fundamental Science and Technology, Keio University,
3-14-1 Hiyoshi, Kohokuku, Yokohama, 223-8522, Japan*

⁶*Quantum Information Science Program, Canadian Institute for Advanced Research, Toronto, ON, M5G 1Z8, Canada*

Quantum computation with electron spin qubits requires coherent and efficient manipulation of these spins, typically accomplished through the application of alternating magnetic or electric fields for electron spin resonance (ESR). In particular, electrical driving allows us to apply localized fields on the electrons, which benefits scale-up architectures. However, we have found that Electric Dipole Spin Resonance (EDSR) is insufficient for modeling the Rabi behavior in recent experimental studies. Therefore, we propose that the electron spin is being driven by a new method of electric spin qubit control which generalizes the spin dynamics by taking into account a quadrupolar contribution of the quantum dot: electric quadrupole spin resonance (EQSR). In this work, we explore the electric quadrupole driving of a quantum dot in silicon, specifically examining the cases of 5 and 13 electron occupancies.

INTRODUCTION

Qubits, the fundamental building block of quantum computers, work by storing quantum information in two quantum states. Therefore, implementations of a quantum computer are possible as long as there are two quantum states (for each qubit) that can be coherently controlled and manipulated to interact with other qubits. Such implementations include electron spin qubits implemented using silicon Metal-Oxide Semiconductor (MOS) technology, which offer numerous advantages. High-fidelity quantum operations have been demonstrated in silicon [1–6] but the main advantage over other qubit technologies is the ability to leverage existing MOS technology. That allows us to build a quantum processor with up to billions of qubits that will be needed to create a universal quantum computer, thus solving problems that would otherwise be too costly for classical computers [7, 8]. The large number of qubits allows quantum error correction algorithms to be implemented, which protect fragile qubits from external sources of noise that can destroy quantum information [9].

Electron spins can be coherently controlled using a microwave source to generate an AC magnetic field resonant with the electronic energy level splitting due to the Zeeman effect [7]. However, using the magnetic field for individual qubit addressability can be problematic because the field is not localized in space. There are

current research efforts to address this problem by using an “always on” global magnetic field [10–12] such as the recently proposed SMART protocol [13–16].

Alternatively, electric driving offers another solution to this problem because electric fields are much more localized. The electron, however, requires a position and/or momentum-dependent magnetic field to couple the spin degree of freedom to the electric field. This coupling is commonly called spin orbit coupling (SOC) and can be realized with an external micromagnet [17–20], or with intrinsic SOC in silicon MOS heterostructures [21, 22], enabling Rabi frequencies up to tens of megahertz [1], which can be an order of magnitude faster compared to the typical magnetic electron spin resonance (ESR) drive [23]. There have also been novel schemes of electric driving to enhance its effect [24], as well as in-depth studies of achieving high-fidelity control [25]. However, one key advantage of using intrinsic SOC over the micromagnet is the reduction of engineering challenges in scale up [7]. The most common way to electrically drive a qubit is called Electric Dipole Spin Resonance (EDSR), where Rabi frequencies are promoted by an alternating electric field coupled with the electron orbital degree of freedom in the dipolar approximation.

In a demonstration of electrically driven multielectron spin qubits using MOS quantum dots [26], it was shown that a multielectron dot not only mitigates charge

noise and disorder [27], but also allows for an order of magnitude enhancement in Rabi frequency compared to a single electron [28]. In particular, with 5 and 13 electrons, a higher quality factor was observed. This is a significant step towards having fault-tolerant qubits, and therefore, we seek to understand and reliably reproduce this behavior in a scale-up architecture.

In this paper, we develop a theoretical model based on the experimental results obtained in Ref. [26]. We begin with a model describing the electric driving of orbital states which controls the spin-orbital character of driven states via the electrostatic gates [22]. Here, we add to the model by arguing that the EDSR description is not sufficient to describe the observed enhancements in Rabi frequency of multielectron dots with > 3 electrons, and we propose a new method named ‘‘Electric Quadrupole Spin Resonance’’ (EQSR).

In the following sections, we first provide a model of the device reported in Ref. [26], making explicit the states that form the spin-orbit qubit for the 5 electrons case and how that leads to EQSR coupling. Then, we present theoretical evidence for EQSR by comparing the theoretical results of this modeling with the experimental results. Finally, we conclude by discussing how we can leverage EQSR in the future.

EQSR THEORY AND MODEL

Microscopic Model

In this section, we begin by building an effective Hamiltonian that describes the system reported in Ref. [26]. We will model the dot with an effective single-particle 2D Hamiltonian that describes the low energy physics as follows:

$$H_{\text{DC}} = H_{\text{xy}} + H_{\text{Zee}} + H_{\text{SO}}. \quad (1)$$

The name DC refers to the static parts of the physics - later we will look at the AC driving terms. This is a simplified description of the system, that illustrates the core physics presented here. The complete Hamiltonian is shown in the Supplementary Material [29] with additional terms relevant to the system that are necessary for fitting but not for the EQSR description.

Let us examine the different components that make up H_{DC} . The orbital Hamiltonian (deduced from COMSOL electrostatic simulations) and the kinetic energy (from silicon band structure) in the xy plane are given by

$$H_{\text{xy}} = \frac{1}{2m_t}(p_x^2 + p_y^2) + \frac{1}{2}m_t\omega_y^2(\delta^2x^2 + y^2), \quad (2)$$

where m_t is the transverse effective mass in the Δ valley of silicon, $\delta \equiv \omega_x/\omega_y$ describes the ellipticity of the parabolic confinement ($\delta = 1$ corresponds to a perfectly

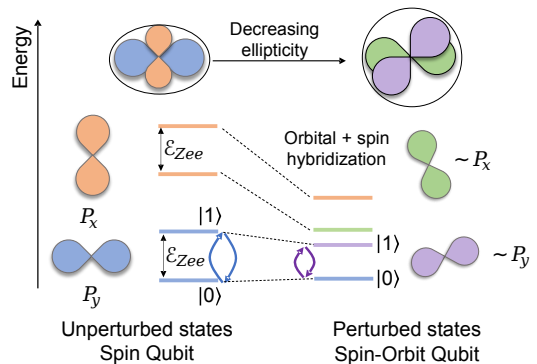


FIG. 1. **Schematic of p-orbital-like states.** As the ellipticity of the electrostatic potential decreases, SOC hybridization of the orbital and spin characters of the states increases, forming a spin-orbit qubit.

circular dot) and $p_{x(y)}$ is the kinetic momentum in the x(y) direction. The spin degree of freedom enters via the Zeeman Hamiltonian $H_{\text{Zee}} = \frac{g\mu_B}{2}\mathbf{B}_0 \cdot \boldsymbol{\sigma}$, with $\mathbf{B}_0 = -B_0\hat{y}$ being a static uniform magnetic field. These two components can be treated as the unperturbed part of the Hamiltonian, and their eigenstates written as $|n, s\rangle$, where $n \in \{S, P_x, P_y, \dots\}$ denotes the 2D quantum harmonic oscillator orbital and $s \in \{\uparrow, \downarrow\}$ denotes the spin state.

The spin-orbit component H_{SO} is considered as a perturbation to $H_{\text{xy}} + H_{\text{Zee}}$. It promotes a hybridization of orbital and spin degrees of freedom between the unperturbed eigenstates $|n, s\rangle$. In this analysis, it can be written as

$$H_{\text{SO}} = \alpha \underbrace{(k_x\sigma'_z + k_y\sigma'_x)}_{h_{\text{R}}} + \beta \underbrace{(-k_x\sigma'_z + k_y\sigma'_x)}_{h_{\text{D}}}, \quad (3)$$

where $h_{\text{R}}, h_{\text{D}}$ are the Rashba and Dresselhaus terms with respective coefficients α, β which arise due to the lowered symmetry of the heterostructure and Si/SiO₂ interface respectively [30]. σ' indicates the Pauli matrices in the spin coordinates as opposed to the real space coordinates and crystallographic axes. The relations between the different coordinates in the system are described in the Supplementary Material [29] and are consistent with the definition of H_{Zee} .

In the 5-electron experiment, the qubit is defined by the unperturbed states $|0\rangle_{\text{unp}} = |P_y, \uparrow\rangle$ and $|1\rangle_{\text{unp}} = |P_y, \downarrow\rangle$. However, H_{SO} couples the different orbital states, resulting in these states becoming,

$$\begin{aligned} |0\rangle &= \mathcal{N}_0(|P_y, \uparrow\rangle + a_0|S, \downarrow\rangle + b_0|P_x, \downarrow\rangle + \dots) \sim |P_y, \uparrow\rangle, \\ |1\rangle &= \mathcal{N}_1(|P_y, \downarrow\rangle + a_1|S, \uparrow\rangle + b_1|P_x, \uparrow\rangle + \dots) \sim |P_y, \downarrow\rangle, \end{aligned} \quad (4)$$

where a_0 comes from first order effect of H_{SO} (from the transition $|P_y, \uparrow\rangle \xrightarrow{k_y\sigma'_x} |S, \downarrow\rangle$), b_0 comes from second order effect of H_{SO} (from the transition $|P_y, \uparrow\rangle \xrightarrow{k_y\sigma'_x}$

$|S, \downarrow\rangle \xrightarrow{k_x \sigma'_z} |P_x, \downarrow\rangle$), and \mathcal{N}_0 is a normalization constant. In a similar fashion the coefficients a_1 , b_1 and \mathcal{N}_1 are defined. The approximation on the right hand side of the equation indicates that the original, unperturbed states are still the most dominant component. The states in Eq. (4) differ both by spin and orbit degrees of freedom and the hybridization promoted by the spin-orbit Hamiltonian is increased when the dot ellipticity decreases (that is, when δ approaches 1), as we will analyze in the next section. Fig. 1 shows a schematic of this hybridization for p-orbital states.

Based on Eq. (3) and the coupling pathways of the states via H_{SO} , we can determine that the $a_{0(1)}$ coefficients are proportional to $\alpha + \beta$ and the $b_{0(1)}$ coefficients are proportional to $\alpha^2 - \beta^2$. These proportionalities lead to different dependencies of the Rabi speed-up on spin-orbit coupling.

Electric Quadrupole Spin Resonance (EQSR)

Now that we have described the DC component of the Hamiltonian, we will describe the AC driving component. An alternating electric field $\mathbf{E} = E_y \cos(\omega t) \hat{y}$ interacts with an electron according to the following Hamiltonian:

$$H_{AC}^{\text{EDSR}}(t) = |e|E_y y \cos(\omega t), \quad (5)$$

which allows spin-flip processes with the Rabi frequency Ω given by

$$\hbar\Omega_{\text{EDSR}} = |\langle 0|eE_y y|1\rangle|. \quad (6)$$

This method of driving is called Electric Dipole Spin Resonance (EDSR). With 5 electrons present in the dot, the states $|0\rangle$ and $|1\rangle$ are those described in Eq. (4), respectively. Therefore, the Rabi frequency would depend on the $a_{0(1)}$ coefficients, since the \hat{y} operator connects states differing in one orbital excitation in the y direction, in this case, the states $|P_y\rangle$ and $|S\rangle$. This means that a Rabi frequency enhancement would only occur when $a_{0(1)}$ are large, i.e. when the $|P_y\rangle$ and $|S\rangle$ orbitals come close in energy, enabling spin-orbit coupling to hybridize the two in a significant fraction. However, the large measured orbital splitting of ~ 4 meV shows that this cannot be the case, indicating that EDSR cannot be responsible for the observed Rabi enhancement.

Then, what can cause the enhancement? The experiments give us two clues. First, no enhancement is observed for a single electron dot [26], suggesting that the enhancement might depend on a property of the P or D orbitals, not present in the S orbitals. The main difference here is the 2- or 3-fold orbital degeneracy.

Second, as the multi-electron dot is tuned towards the degeneracy point (by increasing the electrostatic gate voltage V_{G2}), the lateral electrostatic confinement

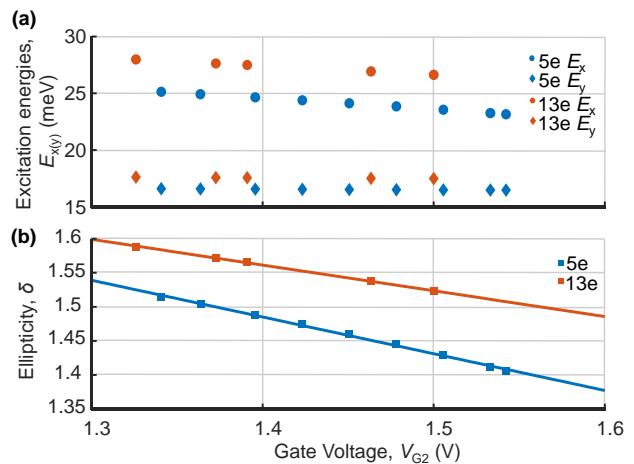


FIG. 2. **Ellipticity and orbital energies.** (a) Plot of the extracted orbital excitation energies $\mathcal{E}_{x(y)} = \hbar\omega_{x(y)}$ against V_{G2} via real-space simulations of the single particle states given an electrostatic potential simulated with COMSOL. (b) Plot of the ellipticity of the dot $\delta \equiv \frac{\mathcal{E}_x}{\mathcal{E}_y}$ against V_{G2} for the 5e configuration in Figs. 3(g-i) and 13e configuration in Figs. 3(j-l) of Ref. [26]. Linear slopes are also shown. Ellipticities were obtained from calculations of energies shown in (a).

is altered. We confirm this via real-space simulations of the COMSOL electrostatic simulations of the device at the operating point, extracting only the single-particle states from electronic structure simulation tools [31]. From the simulations, we obtained the excitation energies $\mathcal{E}_x = \hbar\omega_x$ (circles) and $\mathcal{E}_y = \hbar\omega_y$ (diamonds) in the 5 (blue) and 13 (red) electron regimes, plotted in Fig. 2(a). All the energy traces appear to be linear with the gate voltage. We also plot in Fig. 2(b) the extracted ellipticity, δ , by taking the ratio between \mathcal{E}_x and \mathcal{E}_y in both the 5 and 13 electron configurations (blue and red respectively). We observe that δ varies linearly as a function of gate voltage V_{G2} . This is also further confirmation that no significant Rabi enhancement can occur in the electric dipole spin resonance regime, since ω_y does not vary significantly with the shape of the dot (and neither does ω_x vary enough to cause this enhancement), given that $\Omega \propto y$ and $y \propto \frac{1}{\sqrt{\omega_y}}$. Furthermore, from Fig. 2(b), it is found that the degeneracy point is only achieved when the dot becomes more circular (δ approaching unity as excitation energies decrease), which is opposite to the expected electric dipole effect.

In order to account for these observations in Fig. 2, our model should include the second order Taylor expansion of the driving electric field, or in other words, the quadrupole field

$$Q_{xy} = -\frac{\partial^2 V}{\partial x \partial y} = \frac{\partial E_y}{\partial x} \quad (7)$$

that couples to the qubit via the driving term $H_{AC}^{\text{EQSR}}(t) = |e|Q_{xy}xy \cos(\omega t)$. The full AC Hamiltonian

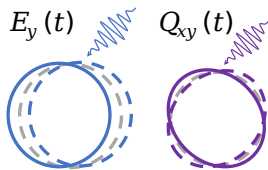


FIG. 3. **Cartoon of the effects of dipolar and quadrupolar electric fields.** An AC quadrupole field results in a dilation/contraction of the electrostatic potential in orthogonal axes whereas an AC dipole electric field results in a shift.

is now extended as

$$H_{AC}(t) = (|e|E_y y + |e|Q_{xy}xy) \cos(\omega t) \quad (8)$$

which at resonance gives rise to what we call Electric Quadrupole Spin Resonance (EQSR), in analogy to Electric Dipole Spin Resonance. A schematic of how the quadrupole driving field affects the electrostatic potential can be found in Fig. 3.

The Rabi frequency will now be given by

$$\begin{aligned} \hbar\Omega &= |\langle 0|eE_y y + eQ_{xy}xy|1\rangle| \\ &\propto |a_1 \langle P_y, \uparrow |E_y y|S, \uparrow\rangle + a_0^* \langle S, \downarrow |E_y y|P_y, \downarrow\rangle + \\ &\quad b_1 \langle P_y, \uparrow |Q_{xy}xy|P_x, \uparrow\rangle + b_0^* \langle P_x, \downarrow |Q_{xy}xy|P_y, \downarrow\rangle + \dots|. \end{aligned} \quad (9)$$

Here, we see that the Rabi frequency enhancement can also be promoted by the second-order perturbation terms of the states $|0\rangle$ and $|1\rangle$. In fact, as the energy difference between the P_x and P_y orbitals approaches that of the Zeeman splitting, which can be achieved by tuning the gate voltages, the coefficient $|b_i|$ grows larger. Therefore, this treatment may predict the enhancement observed within this regime. For the 13-electron experiment, this quadrupole driving will also couple the D_{xy} with D_{yy} or D_{xx} orbitals.

Although quadrupole coupling is expected due to the non-uniformity of the electric field produced by the gates, it is often been neglected in calculations of the Rabi frequency. The Q_{xy} term in the Hamiltonian is the only term to directly couple the P_x, P_y orbitals, as well as the D_{xy}, D_{yy} ones, which can account for the observed Rabi enhancement. There are other components of the quadrupole field in the driving term H_{AC} , but they do not offer direct coupling between the orbitals and therefore become negligible in our description.

We will conclude this section with some intuition on the influence of the quadrupole Q_{xy} term on the dot. Whereas electric dipole spin resonance causes a lateral oscillation of the dot, EQSR causes a dilation/contraction of potential along the $x = \pm y$ axes (see Fig. 3). Another way of thinking about this driving term is that it has an $x = y$ symmetry axis, which allows it to couple orbitals of opposite x and y symmetry. COMSOL simulations yield $Q_{xy}/E_y = 1.2 \times 10^{-3} \text{ nm}^{-1}$,

a ratio that we kept fixed when fitting our model to the experiment. Our dot occupies a region of linear size $L \sim 20 \text{ nm}$, and therefore we see that $Q_{xy}L/E_y \ll 1$, as required for the validity of the multipolar expansion.

RESULTS AND DISCUSSION

In this section, we show that EQSR allows us to explain the experimental results reported by Ref. [26]. Diagonalizing H_{DC} [Eq. (1)] allows us to obtain both the ESR frequency given by $\hbar f_{\text{ESR}} = \mathcal{E}_1 - \mathcal{E}_0$, and the Rabi frequency Ω given by Eq. (9). We perform a least-squares fit to the experimental data, simultaneously fitting both the qubit and Rabi frequencies as a function of the ellipticity of the dot δ , with results shown in Fig. 4. A similar fitting protocol was used in Ref. [22].

We first examine the results of the 5-electron regime, with the resulting energy levels shown in Fig. 4(a). Here, we are largely concerned with the P_x and P_y orbitals, given that we expect the valence electron to be sitting in the P_x orbital based on electron-filling principles. We can obtain the qubit frequencies by calculating the energy difference between the ground and the first excited state, which we plot in Fig. 4(b). Here, the theoretical estimate is presented in red, contrasting with the experimental data in black. Finally, we can calculate the resulting Rabi frequency based on these qubit parameters, which is plotted in Fig. 4(c). The solid and dashed blue lines indicate respectively the Rabi frequency with and without EQSR contributions. It is important to highlight that this was plotted using the parameters fitted for the model that included EQSR, so it is trivial that the line representing only EDSR would not be a good fit. Our conclusions arrive from the fact that we tried as well to do a fitting procedure that does not include EQSR, but we could not reproduce the enhancement that follows the experimental data near the degeneracy point. This supports our theoretical hypothesis that EQSR is required to explain the Rabi frequency speed-ups.

We obtained similar results in the 13-electron regime, with the main difference being the orbitals on which the electric drive is acting, which are the D orbitals in this case. We show the D orbital energy levels, the qubit frequency fits, and the Rabi frequency fits in Figs. 4(d), (e), and (f) respectively. In this case, the qubit frequency is similarly defined as the difference between the ground and first excited energy of the D orbital energy levels. In Fig. 4(f), we show that the enhancement in Rabi frequency can be mapped by the Hamiltonian with the inclusion of EQSR.

Therefore, in both the 5 electron and 13 electron cases, we demonstrate our ability to capture the behavior of the Rabi frequency speed-up. We stress that a quantitative correspondence between the experimental data and the theoretical fits is not the scope of this

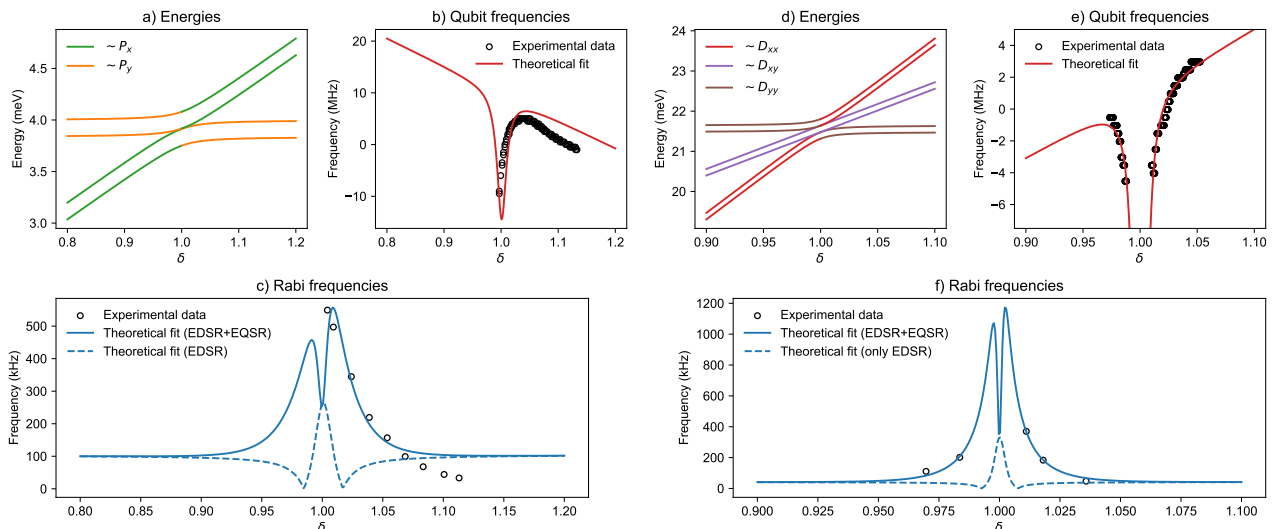


FIG. 4. **Fitted EQSR model.** (a) Energies of the P_x and P_y orbitals with the lowest two being the ones driven by EQSR. (b) Qubit frequency spectrum of the 5 electron regime, with the measured data in black and the fitted line in red. (c) Rabi frequency measured in the 5 electron regime, with the measured data in black and the fitted line in blue. The dashed line indicates the model prediction if only the electric dipole effect is accounted for. (d) Energies of the D orbitals, with the lowest two being those driven by EQSR. (e) Qubit frequency spectrum of the 13 electron regime, with the measured data in black and the fitted line in red. (f) Rabi frequency measured in the 13-electron regime, with the measured data in black and fitted line in blue. The dashed line indicates the model prediction if only the electric dipole effect is accounted for. All x -axis labels here are the ellipticity $\delta \equiv \frac{\epsilon_x}{\epsilon_y}$.

paper, and the main point is rather to show how the electrical quadrupole is necessary to explain the Rabi enhancement near the degeneracy point. The challenges in these fittings arise from several factors, including, but not limited to, insufficient experimental data points and having a multitude of parameters. We will discuss the technical aspects of the fitting protocol in greater detail in the Supplementary Material.

From a physics point of view, we know that the ESR frequency of the qubit can be susceptible to the surface roughness at the silicon-silicon dioxide interface [32] as well as nuclear spins [33], and that is difficult to account for in fittings such as the one performed here. We would have to include some form of non-linear voltage dependence in the qubit frequency.

Finally, we see from Eq. (9) that while Rabi frequency promoted by EDSR depends on $a_{0(1)} \propto \alpha + \beta$, the Rabi enhancement promoted by EQSR depends on $b_{0(1)} \propto \alpha^2 - \beta^2$. This means that in order to improve Rabi frequencies next to the degeneracy point using intrinsic spin-orbit coupling, the latter relation between Rashba and Dresselhaus coefficients should be looked upon. If the difference between the square of the two terms are large enough, the addition of a micromagnet could be rendered unnecessary, which is desirable for scale-up architectures.

The experimental results in Ref. [26] show a clear correlation between the nonlinear bend of the qubit

frequencies and the one order of magnitude increase in the Rabi frequencies of P and D orbitals. As we have shown here, both features can be explained within an effective single-particle theory if the quadrupole coupling is being taken into account. Our fits show the rising of Rabi frequency as dot shape becomes more circular, i.e. as we approach the anti-crossing point, therefore indicating clearly the role of EQSR in enhancing the Rabi frequency close to the degeneracy as a function of the ellipticity. In summary, we believe that the technique of quadrupole spin resonance opens up new pathways for coherent spin control with multi-electron dots and can become an ally in the quest for scalable quantum computation.

ACKNOWLEDGMENTS

We acknowledge support from the Australian Research Council (FL190100167, CE170100012, and IM230100396) and the US Army Research Office (W911NF-23-10092). The views and conclusions contained in this document are those of the authors and should not be interpreted as representing the official policies, either expressed or implied, of the Army Research Office or the US Government. M.K.F. and J.D.C. acknowledges support from Sydney Quantum Academy. L.A.L. and P.H.P. acknowledge funding

from the Brazilian agencies Conselho Nacional de Desenvolvimento Científico e Tecnológico (CNPq) and Coordenação de Aperfeiçoamento de Pessoal de Nível Superior (CAPES).

* These authors contributed equally

† Current Address: Quantum Motion, 9 Sterling Way, London N7 9HJ, United Kingdom

‡ Current Address: Laboratory for Solid State Physics, ETH Zurich, CH-8093 Zurich, Switzerland

§ Current Address: IQM Quantum Computers, Espoo 02150, Finland

¶ mengke.feng@unsw.edu.au

** a.saraiva@unsw.edu.au

- [1] J. Yoneda, K. Takeda, T. Otsuka, T. Nakajima, M. R. Delbecq, G. Allison, T. Honda, T. Kodera, S. Oda, Y. Hoshi, N. Usami, K. M. Itoh, and S. Tarucha, *Nature Nanotechnology* **13**, 102 (2017).
- [2] W. Huang, C. H. Yang, K. W. Chan, T. Tantt, B. Hensen, R. C. C. Leon, M. A. Fogarty, J. C. C. Hwang, F. E. Hudson, K. M. Itoh, A. Morello, A. Laucht, and A. S. Dzurak, *Nature* **569**, 532 (2019).
- [3] M. T. Maźzik, S. Asaad, A. Youssry, B. Joecker, K. M. Rudinger, E. Nielsen, K. C. Young, T. J. Proctor, A. D. Baczewski, A. Laucht, *et al.*, *Nature* **601**, 348 (2022).
- [4] A. Noiri, K. Takeda, T. Nakajima, T. Kobayashi, A. Sammak, G. Scappucci, and S. Tarucha, *Nature* **601**, 338 (2022).
- [5] X. Xue, M. Russ, N. Samkharadze, B. Undseth, A. Sammak, G. Scappucci, and L. M. Vandersypen, *Nature* **601**, 343 (2022).
- [6] T. Tantt, W. H. Lim, J. Y. Huang, N. Dumoulin Stuyck, W. Gilbert, R. Y. Su, M. Feng, J. D. Cifuentes, A. E. Seedhouse, S. K. Seritan, *et al.*, *Nature Physics*, 1 (2024).
- [7] M. Veldhorst, H. G. J. Eenink, C. H. Yang, and A. S. Dzurak, *Nature Communications* **8**, 10.1038/s41467-017-01905-6 (2017).
- [8] A. Saraiva, W. H. Lim, C. H. Yang, C. C. Escott, A. Laucht, and A. S. Dzurak, *Advanced Functional Materials* **32**, 2105488 (2022).
- [9] S. J. Devitt, W. J. Munro, and K. Nemoto, *Reports on Progress in Physics* **76**, 076001 (2013).
- [10] A. Laucht, J. T. Muhonen, F. A. Mohiyaddin, R. Kalra, J. P. Dehollain, S. Freer, F. E. Hudson, M. Veldhorst, R. Rahman, G. Klimeck, K. M. Itoh, D. N. Jamieson, J. C. McCallum, A. S. Dzurak, and A. Morello, *Science Advances* **1**, e1500022 (2015).
- [11] E. Vahapoglu, J. P. Slack-Smith, R. C. Leon, W. H. Lim, F. E. Hudson, T. Day, T. Tantt, C. H. Yang, A. Laucht, A. S. Dzurak, *et al.*, *Science Advances* **7**, eabg9158 (2021).
- [12] E. Vahapoglu, J. Slack-Smith, R. C. Leon, W. H. Lim, F. Hudson, T. Day, J. Cifuentes, T. Tantt, C.-H. Yang, A. Saraiva, *et al.*, *npj Quantum Information* **8**, 126 (2022).
- [13] I. Hansen, A. E. Seedhouse, A. Saraiva, A. Laucht, A. S. Dzurak, and C. H. Yang, *Physical Review A* **104**, 062415 (2021).
- [14] A. E. Seedhouse, I. Hansen, A. Laucht, C. H. Yang, A. S. Dzurak, and A. Saraiva, *Physical Review B* **104**, 235411 (2021).
- [15] I. Hansen, A. E. Seedhouse, K. W. Chan, F. Hudson, K. M. Itoh, A. Laucht, A. Saraiva, C. H. Yang, and A. S. Dzurak, *Applied Physics Reviews* **9** (2022).
- [16] I. Hansen, A. E. Seedhouse, S. Serrano, A. Nickl, M. Feng, J. Y. Huang, T. Tantt, N. Dumoulin Stuyck, W. H. Lim, F. E. Hudson, *et al.*, *Nature Communications* **15**, 7656 (2024).
- [17] T. Obata, M. Pioro-Ladrière, Y. Tokura, Y.-S. Shin, T. Kubo, K. Yoshida, T. Taniyama, and S. Tarucha, *Physical Review B* **81**, 085317 (2010).
- [18] K. Takeda, J. Kamioka, T. Otsuka, J. Yoneda, T. Nakajima, M. R. Delbecq, S. Amaha, G. Allison, T. Kodera, S. Oda, *et al.*, *Science advances* **2**, e1600694 (2016).
- [19] P. Huang and X. Hu, *npj Quantum Information* **7**, 162 (2021).
- [20] E. Kawakami, P. Scarlino, D. R. Ward, F. Braakman, D. Savage, M. Lagally, M. Friesen, S. N. Coppersmith, M. A. Eriksson, and L. Vandersypen, *Nature nanotechnology* **9**, 666 (2014).
- [21] T. Tantt, B. Hensen, K. W. Chan, C. H. Yang, W. W. Huang, M. Fogarty, F. Hudson, K. Itoh, D. Culcer, A. Laucht, A. Morello, and A. Dzurak, *Physical Review X* **9**, 10.1103/physrevx.9.021028 (2019).
- [22] W. Gilbert, T. Tantt, W. H. Lim, M. Feng, J. Y. Huang, J. D. Cifuentes, S. Serrano, P. Y. Mai, R. C. Leon, C. C. Escott, *et al.*, *Nature Nanotechnology*, 1 (2023).
- [23] J. J. Pla, K. Y. Tan, J. P. Dehollain, W. H. Lim, J. J. L. Morton, D. N. Jamieson, A. S. Dzurak, and A. Morello, *Nature* **489**, 541 (2012).
- [24] J. D. Teske, F. Butt, P. Cerfontaine, G. Burkard, and H. Bluhm, *Physical Review B* **107**, 035302 (2023).
- [25] M. Rimbach-Russ, S. G. Philips, X. Xue, and L. M. Vandersypen, *Quantum Science and Technology* **8**, 045025 (2023).
- [26] R. Leon, C. H. Yang, J. Hwang, J. C. Lemyre, T. Tantt, W. Huang, K. W. Chan, K. Tan, F. Hudson, K. Itoh, *et al.*, *Nature communications* **11**, 797 (2020).
- [27] E. Barnes, J. P. Kestner, N. T. T. Nguyen, and S. D. Sarma, *Physical Review B* **84**, 10.1103/physrevb.84.235309 (2011).
- [28] H. E. Ercan, C. R. Anderson, S. Coppersmith, M. Friesen, and M. F. Gyure, *arXiv preprint arXiv:2303.02958* (2023).
- [29] See Supplementary Material for more details.
- [30] L. E. Golub and E. L. Ivchenko, *Physical Review B* **69**, 115333 (2004).
- [31] Z. Wang, M. Feng, S. Serrano, W. Gilbert, R. C. Leon, T. Tantt, P. Mai, D. Liang, J. Y. Huang, Y. Su, *et al.*, *Advanced Materials*, 2208557 (2023).
- [32] J. D. Cifuentes, T. Tantt, W. Gilbert, J. Y. Huang, E. Vahapoglu, R. C. Leon, S. Serrano, D. Otter, D. Dunmore, P. Y. Mai, *et al.*, *Nature Communications* **15**, 4299 (2024).
- [33] P. Stano, T. Nakajima, A. Noiri, S. Tarucha, and D. Loss, *Physical Review B* **108**, 10.1103/physrevb.108.155306 (2023).